Available online at www.sciencedirect.com
SCIENCE DIRECT
ELSEVIER
Polymer 46 (2005) 8210–8221
polymer
www.elsevier.com/locate/polymer

Influence of molecular parameters on high-strain deformation of polyethylene in the plane-strain compression. Part I. Stress–strain behavior

Z. Bartczak[a,*], M. Kozanecki[b]

[a]Department of Polymer Physics, Centre of Molecular Macromolecular Studies, Polish Academy of Sciences, Sienkiewicza 112, 90-363 Lodz, Poland
[b]Department of Molecular Physics, Technical University of Lodz, Zeromskiego 116, 90-924 Lodz, Poland

Received 18 April 2005; received in revised form 22 June 2005; accepted 22 June 2005
Available online 21 July 2005

Abstract

Deformation behavior of several polyethylenes and ethylene-based copolymers with various molecular architecture (linear and branched polyethylene, ethylene based copolymers), and a broad range of molecular mass and its distribution, was studied. Due to the differences in molecular characteristic, this series exhibited a relatively broad range of crystallite sizes as well as crystallinity level, varying from less than 10% up to more than 70%.

The samples of polyethylenes and copolymers were subjected to high-strain compression in the plane-strain conditions. The true strain exceeded frequently the value of 2 (a corresponding deformation ratio up to around 10). Plastic deformation to high strain was associated with an intense strain-hardening, leading to very high stress, above 500 MPa. It was found that the yield behavior and the stress of plastic flow depended mainly on the amount of amorphous and crystalline components and on the thickness of lamellar crystals, while the strain hardening behavior depended primarily on the density of chain entanglements in the amorphous component, which in turn was controlled by molecular mass and chain architecture of the polymer, both influencing the process of network modification upon crystallization.

Keywords: Polyethylene; Plastic deformation; Chain entanglements

1. Introduction

Many semicrystalline polymers can undergo large plastic strains by extensional flow in tension or compression, resulting in anisotropic end products of very attractive mechanical properties [1]. It has been appreciated that while all semicrystalline polymers are made up of amorphous and crystalline components, it is the plastic properties of a crystalline component that govern the overall deformation behavior and establish the final anisotropic properties. Particular attention given in the past to the deformation of a crystalline component resulted in a broad knowledge of the mechanisms employed [2–4]. However, there is considerably less understanding of the role of an amorphous component in the deformation sequence as well as micro-mechanisms involved and interactions between adjacent layers of crystalline and amorphous components, which are tightly connected by covalent bonds and must deform simultaneously due to continuity condition.

An amorphous component consists of highly entangled chains forming a continuous network. The entanglements and crystallites adjacent to the amorphous layers constitute physical cross-links of that network. The entanglements existing in a molten polymer are usually not resolved by the crystallization process. What is important, most of them is merely shifted into amorphous interlamellar layers [5]. This means redistribution, typically on the length scale of about 10 nm and modification of the local network density, but globally, the isotropic entangled network of the melt is retained after crystallization. That network should manifest itself in high reversibility of the deformation, which in fact, is frequently observed experimentally.

The number of entanglements persisting in the amorphous phase after sample crystallization depends actually on the conditions of crystallization process and,

* Corresponding author. Tel.: +48 42 680 3237; fax: +48 42 684 7126.
E-mail address: bartczak@bilbo.cbmm.lodz.pl (Z. Bartczak).

0032-3861/$ - see front matter © 2005 Elsevier Ltd. All rights reserved.
doi:10.1016/j.polymer.2005.06.100

therefore, can be modified in a certain range. For example, the density of entanglements can be considerably reduced in the samples crystallized carefully from dilute solution [6,7], or in the samples of a relatively low molecular weight crystallized slowly from the melt [8]. Another possibility of fabrication of material with lowered density of entanglements offers crystallization during polymerization [9]. The ability of some polymers to crystallize in chain-extended fashion under elevated pressure, like PE or PVDF, also allows for a reduction of the number of entanglements at appropriate crystallization conditions [10]. However, apart from these special cases, the number of entanglements in solidified semicrystalline polymer usually remains high, while the local density of entanglements within amorphous layers can be similar to or even higher than the respective density in the melt. This is especially true for fast-crystallized samples of polymers of moderate or high molecular weight, in which the rate of disentanglement driven by crystallization is usually much lower than the overall rate of crystallization. At such conditions nearly all pre-existing entanglements are only rejected by growing crystallites into surrounding amorphous layers rather than be resolved.

Modification of the local entanglement density resulting from crystallization process leads to an essential difference between the molecular network within amorphous layers of semicrystalline polymers and that present in amorphous polymers, in which the entanglement density depends solely on the properties of the chains, and depends neither on their length nor thermal history of the sample [11]. On the contrary, the density of the network in a solid semicrystalline polymer is expected to vary with both molecular weight and conditions of its crystallization.

Recently Strobl et al. [12–17] focused on these aspects of the deformation of semicrystalline polymers, which are related to the presence of the molecular network. They studied the deformation and recovery behavior of several semicrystalline polymers, including a series of polyethylenes [12–15] and found a quite simple general deformation strain-dependent scheme, which was followed by all polymers studied. Along the true stress-true strain curves the differential compliance, recovery behavior as well as the crystalline texture change simultaneously at well-defined strains. Four characteristic transformation points were identified. Among these, two high-strain transformation (point C- the beginning of crystallite fragmentation and fibril formation and D- the onset of chain disentanglement) were found to be related to the molecular network within amorphous phase.

The goal of investigations presented in this paper was to study the high-strain deformation behavior of semicrystalline polymers with special attention given to the role of the amorphous phase and its topological structure. For this purpose materials demonstrating a notable variation in the amount and properties of the amorphous phase were studied, yet a similar structure of the crystalline component and supermolecular structure were needed as the object of studies. To achieve that goal, a series of polyethylene and ethylene-based copolymer samples was selected to cover a possibly broad range of molecular mass as well as chain architecture. They demonstrated a broad range of crystallinity and were also expected to show different topological structure of the amorphous component. In order to minimize any possible influence of the supermolecular structure on mechanical response, all samples were prepared under identical conditions resulting in fast crystallization from the melt, which led to the formation of comparable supermolecular structures in all samples.

Most of the deformation studies were performed in the past in uniaxial drawing. However, under a tensile force, a microscopic voiding frequently arises in addition to slip processes. Moreover, the deformation is unstable for most of polymers and drawing conditions, leading to localization of the deformation and eventually to the formation of a macroscopic neck. These phenomena can obscure seriously the real micro-mechanisms involved. To avoid these side effects a cavity-free, plane-strain compression was chosen as a deformation mode. Deformation in this mode proceeds practically homogeneously, without any instability, while kinematically it is similar to tension, leading to axial flow of the polymer in the direction perpendicular to a compressive load [18]. Moreover, the determination of the true stress-true strain behavior is much simpler in the plane-strain compression than in any other deformation mode. Suppression of any cavitation phenomena due to compressive stress components results in deformation to strain and stress usually reasonably higher than in tension, practically without the premature fracture of a sample. This allows to study the deformation behavior in a broader strain range and to avoid any unwanted phenomena, like cavitation or necking, which are inessential from the point of view of the real mechanisms involved. Furthermore, it should be mentioned that constraints imposed on a sample during its compression in the plane-strain experiment eliminate also most of the problems which could be encountered in uniaxial compression (which is also a cavity-free mode), as those related to sample barreling or radial cracking at a very high strain.

Strobl et al. found that the deformation sequence in tension was entirely strain-controlled and practically did not depend on the temperature or deformation rate [13]. Therefore, we decided to start our research at a single temperature and deformation rate.

In this paper, a study of the stress–strain behavior of the series of polyethylenes is reported. A companion paper [19] presents results of the investigations of the post-deformation recovery process of the same materials.

2. Experimental

2.1. Materials and sample preparation

Materials used in this study were the samples of various grades of commercial polyethylene, including five linear

high-density polyethylenes (HDPE) of various molecular mass, two samples of ultra-high molecular mass polyethylene (UHMWPE), five conventional branched polyethylenes of different branching level and molecular mass (LDPE) and four copolymers of ethylene with various contents of butene-1 or octene-1 comonomer (linear low density polyethylenes, LLDPE and ethylene-octene-1 elastomers). One of LLDPE's (LL-1) was synthesized with metallocene catalyst, while the other (LL-2) was produced with the conventional Ziegler–Natta catalyst system. Both ethylene-octene-1 elastomers (E-1, E-2) were of metallocene type. All materials studied are summarized in Table 1.

Samples for mechanical tests, in the form of 50×50 mm plates, 4 mm thick, were prepared by compression molding at $T=190$ °C (230 °C for UHMWPE specimens) and $p=50$ atm. The compressed plates were solidified by fast cooling in iced water. All samples were prepared according to an identical procedure, at the same thermal conditions. Prior to crystallization, all samples were melt-annealed for 10 min, i.e. long enough to erase their thermal history (since all the samples contained stabilizers, their degradation was negligible). Cooling in the iced water provided conditions for fast polyethylene crystallization, which resulted in the formation of a similar supermolecular structure of the investigated materials. Specimens of the size desired for particulate experiment were machined out from the plates. Such machining removed the skin layer in which a structure gradient due to fast cooling conditions was expected. The core parts of the plates, used in all experiments, demonstrated relatively uniform structure as compared to removed skin layers.

2.2. Characterization

2.2.1. DSC

Thermal analysis of the samples was conducted using a TA 2920 DSC apparatus (TA Instruments), indium calibrated. The 5–8 mg specimens were cut out from the core of compression molded sheets. Melting thermograms were recorded at the heating rate of 10°/min, under nitrogen flow. The crystallinity level and length of crystalline stem, l^*, were estimated on the basis of the heat of sample melting recorded during heating from −20 to 180 °C and from the recorded melting temperature, T_m, respectively. For the determination of l^*, the Gibbs–Thompson equation was used [20]:

$$l^* = \frac{2\sigma_e T_m^0}{\Delta h_f (T_m^0 - T_m)} \quad (1)$$

where σ_e is the lamellar basal surface free energy (for PE $\sigma_e = 9\times10^{-6}$ J/cm^2, [21]), Δh_f is the heat of fusion per unit volume (for PE $\Delta h_f = 293$ J/cm^3, [22]), T_m^0 is the extrapolated equilibrium melting temperature (145.5 °C as estimated for infinite molecular mass [23]; $T_m^0 = 145.1$ °C was determined earlier for sample H-1 of relatively low $M_w = 5.7\times10^4$, [24]).

2.2.2. Density

Density of the samples was determined with a gradient

Table 1
Molecular characteristic of polymers studied

Sample code	Manufacturer	M_w (g/mol)	M_w/M_n	Number of branches (1/1000C)	Melt flow index (2.16 kg, 190 °C) (g/10 min)	Density (g/cm^3)
Linear polyethylenes (HDPE, UHMWPE)						
H-1	Quantum	5.74×10^4	3.5	<0.1	6.7	0.9565
H-2	BASF	7.63×10^4	4.4	<0.1	7	0.9567
H-3	BASF	1.2×10^5	3.4	<5	2.3	0.9425
H-4	BASF	1.83×10^5	7.2	<0.2	0.2	0.9560
H-5	BASF	4.78×10^5	12.2	<3	–	0.9528
U-1	Ticona	$\sim2\times10^6$			–	0.9280
U-2	Ticona	$\sim5.5\times10^6$			–	0.9290
Branched polyethylenes (LDPE)						
L-1	BASF	2.5×10^5		20	3.4	0.9223
L-2	BASF	3.3×10^5		24	2.1	0.9217
L-3	BASF	4.5×10^5	13.0	35	0.3	0.9185
L-4	BASF	2.0×10^5	4.0	35	1.6	0.9185
L-5	BASF	4.8×10^4	3.7	35	20	0.9170

Sample code	Manufacturer	M_w (g/mol)	M_w/M_n	Comonomer type	Comonomer content (mol%)	Melt flow index (2.16 kg, 190 °C) (g/10 min)	Density (g/cm^3)
Ethylene copolymers (LLDPE, ethylene–octene rubbers)							
LL-1	Elenac	7.1×10^4	2.4	Butene-1	4.1	2.5	0.9183
LL-2	Elenac	9.2×10^4	4.0	Butene-1	4.1	2.8	0.9180
E-1	Exxon	8.2×10^4	3.7	Octene-1	8.2	3	0.9020
E-2	Dow-DuPont elastomers	3.67×10^5	2.1	Octene-1	14.4	0.5	0.8700

column filled with a mixture of water and ethyl alcohol, covering the density range from 0.85 to 0.98 g/cm^3. The column was thermostated (T=25 °C) and calibrated with 12 glass floats of known density. From density data the degree of crystallinity (volumetric and weight) were calculated using the densities of ρ_a=0.855 g/cm^3 and ρ_c=1.0 g/cm^3 for the amorphous and crystalline phase, respectively [25].

2.2.3. Raman spectroscopy

Low acoustic frequency Raman spectra were also used for the determination of length of the crystalline stem, l^*. The frequency shift of a low acoustic peak with respect to the frequency of the excitation light, $\Delta\nu$, expressed in cm^{-1}, depends on the length of vibrating chain, l^*, and on the velocity of sound along the chain (expressed by $(E_{11}/\rho)^{-1/2}$, E_{11} being Young's modulus of PE crystals in the direction of chain and ρ the density of crystals) in the following way [26]:

$$\Delta\nu = \frac{m}{2l^*c}\left(\frac{E_{11}}{\rho}\right)^{-1/2} \quad (2)$$

where m is the order of the vibrational mode and c is the velocity of light. Assuming the PE crystal density as 1.0 g/cm^3, the E_{11} modulus as 360 GPa (this value was estimated by Rastogi et al. [27] using a sample with known crystal thickness, whereas the theoretical value of E_{11} equals to 405 GPa as it follows from the consideration of C–C bond extension [28]) the length of the crystalline stem in lamellar crystal can be calculated on the basis of the following formula:

$$l^* = \frac{316.2}{\Delta\nu} \quad (3)$$

where l^* is the length of crystalline stem (in nm) and $\Delta\nu$ (in cm^{-1}) is the position of the peak associated with the first order longitudinal acoustic mode (LAM-1) [29].

Low acoustic frequency Raman spectra of crystallized PE samples taken from the core of compression molded plates prepared for mechanical tests, were recorded by means of a Raman spectrometer Z40 (DILOR) with five diffraction grids. The light source was a 120 mW argon laser (λ=514.5 nm).

2.2.4. SAXS

Lamellar structure of raw and deformed samples was probed by a 2D small angle X-ray scattering (2D SAXS). A 1.1 m long Kiessig-type camera was equipped with a tapered capillary (XOS) and pinhole collimator and an imaging plate as a detector (Fuji). The camera was coupled to a X-ray generator (sealed-tube, fine point Cu Kα filtered source operating at 50 kV and 40 mA; Philips). Exposed imaging plates were read with Phosphor-Imager SI system (Molecular Dynamics).

The long period was determined from one-dimensional sections of 2D pattern. It was calculated from the position of the maximum of background and Lorentz corrected curves using Bragg's law.

2.3. Deformation experiments

Plane-strain compression was chosen as the deformation mode throughout this study. The plane-strain compression tests were performed using the loading frame of 5 T capacity (Instron, Model 1114) and a compression tool of the type of a channel-die [18,30], equipped with a load and strain gauges. This compression tool, shown schematically in Fig. 1, was a set of a lower die with a wide rectangular channel cut across the die and an upper plunger fitting the channel in the lower die. The size of the channel in the lower die was 15 mm in width (i.e. along the constrained direction, CD) 6 mm in length (along the flow direction, FD), and 6 mm in depth (along the loading direction, LD). To provide a precise position and guidance of the plunger against the lower die, the lower die was attached to the base steel block, while the plunger was attached to another steel block guided by four solid columns mounted on the base. This fixture is shown schematically in Fig. 1 with a broken line.

The size of specimens used in compression experiments was 15×6×4 mm^3 (CD×FD×LD). The surfaces contacting with a die and plunger were lubricated to reduce friction forces during deformation.

All deformation experiments were performed at a constant speed of the crosshead of the loading frame. The speed of the crosshead was set to 8.3×10^{-4} s^{-1} to get the initial deformation rate of 5%/min. All tests described in this paper were performed at room temperature.

3. Results and discussion

3.1. Properties of the crystalline phase

As demonstrated by SAXS measurements all samples

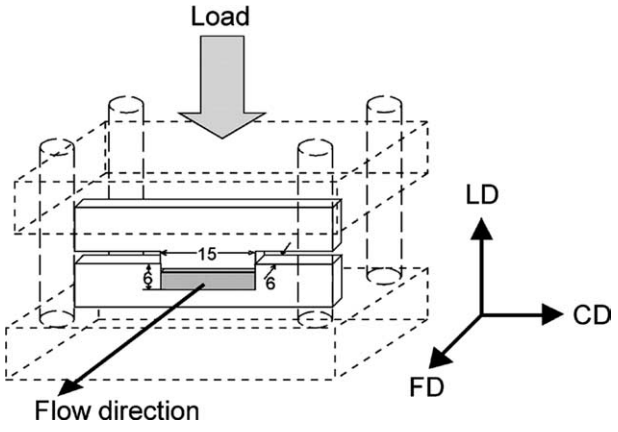

Fig. 1. Deformation tool used for plane-strain compression. The compressed sample is marked gray. The guidance system is shown with a broken line. Dimensions are given in mm.

prepared in this study exhibited lamellar morphology. Moreover, supplementary microscopic observations and light scattering experiments demonstrated that in most of the samples (with the exception of U-1, U2 and E-2) the lamellae were organized in spherulites that filled completely the volume of the sample. The average size of spherulites was different in every sample, varying from a few up to more than 10 μm. That size is governed by primary nucleation, which in turn, for samples crystallized at the same thermal conditions applied in this study was controlled primarily by the number of foreign impurities present in a polymer. In the samples of U-1, U-2 (UHMWPE) and E-2 (ethylene-octene-1 copolymer) the lamellae were distributed randomly and did not form spherulitic structures.

The amount of crystalline and amorphous components, as well as the properties of crystalline component in the samples under study were determined using DSC, density, SAXS and Raman spectroscopy. Fig. 2 presents a few exemplary DSC melting curves. From similar endotherms the temperature of the main melting peak and crystallinity degree were evaluated for all samples studied. Results are presented in Table 2.

The degree of crystallinity was determined independently also by density measurements. The measured densities of the samples are listed in Table 1, while the calculated values of crystallinity are reported in Table 2 next to crystallinity based on DSC data. One can notice a small, systematic deviation of the density-based degree of crystallinity toward higher values as compared to respective values estimated from DSC data. Similar differences of crystallinity estimated from the heat of melting and density are frequently observed for many semicrystalline polymers.

Long period, also presented in Table 2, was determined from small angle X-ray scattering (SAXS) data. The thickness of lamellae, L_c, was estimated then from long period and crystallinity degree (DSC-based; recalculated to the volume contribution).

The length of crystalline stem in the lamellae, l^*, was estimated from temperature of the main melting peak

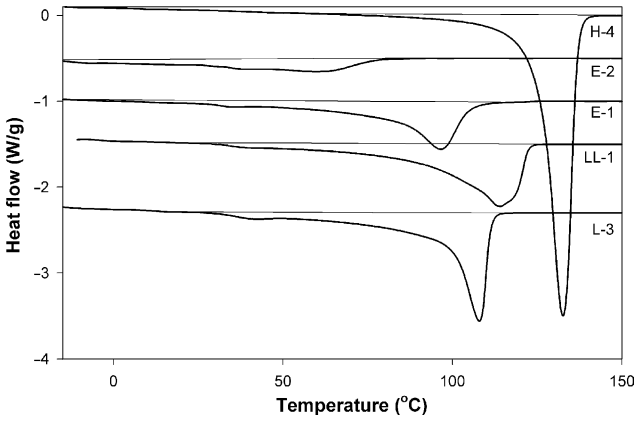

Fig. 2. Representative DSC scans recorded on heating at the rate of 10 °C/min for selected samples, labeled on respective curves. For clarity, the curves were shifted along the heat flow axis.

observed by DSC, and independently from low frequency Raman spectra, as described in Section 2. These data are presented in two last columns of Table 2. A comparison of both data sets demonstrates that there is a systematic deviation towards higher values of l^* determined from Raman spectra as compared with those determined from DSC data. Fig. 3 demonstrates, however, that there is a good linear correlation between both data sets, yet the slope of correlation line is approximately 1.21 instead of being close to 1, as expected. In the evaluation of l^* from Raman spectra it was necessary to choose an appropriate value of Young's modulus of crystals in the direction of chain. We used in our calculations the value of $E_{11}=360$ GPa, as estimated by Rastogi et al. [27]. Our data may suggest that a significantly lower modulus value should be taken for these calculations in order to obtain better agreement with DSC-based estimations. However, to get good agreement with l^* estimated from the melting peak data, one should take an unreasonably low value of Young's modulus of only 206 GPa, which is roughly half of the theoretical value (405 GPa [28]) and is notably lower than most of other experimental estimations (219–360 GPa [27,29,31,32], although values below 200 GPa were also reported, see Ref. [32] for a survey of the existing data). On the other hand, the stem length, as calculated from the DSC data, when compared to lamellar thickness seems to be quite reasonable-the estimated angle between chain direction and lamella normal vary within the range of 30–50° for the entire series of polymers studied, while the use of l^* estimated from Raman spectra (with $E_{11}=360$ GPa) leads to the estimated tilt angle of 50–70°, which is apparently too high. The tilt angle of 34.5° was determined for linear PE by Basset and Hodge [33]. Because of this uncertainty of l^* determined from Raman spectroscopy, we used DSC-based values in further analysis.

3.2. Stress–strain behavior

From the measured load-displacement data the true stress-true strain curves were evaluated. In the plane-strain compression in a channel die the area of sample under load remains constant through the experiment. It is always equal to the area of contact between the sample and plunger. Therefore, the true stress is all the time equal to the nominal stress. The true strain, e, was calculated from the reduction of the specimen dimension along the loading direction (specimen height) according to the following formula (Hencky measure of strain):

$$e = \int_{h_1=h_0}^{h_1=h} \frac{\mathrm{d}h_1}{h_1} = \ln\left(\frac{h_0}{h}\right) = \ln\left(\frac{h_0}{h_0-\Delta h}\right) = \ln(\mathrm{CR}) \quad (4)$$

where h_0 denotes the initial height of the specimen, $h=h_0-\Delta h$ represents its actual height, Δh is the measured

Table 2
Crystallinity degree and properties of crystalline component

Sample code	Temperature of the melting peak T_m (°C)	Degree of crystallinity, X_c, from:		Long period, LP,[a] (nm)	Lamellar thickness, L_c,[b] (nm)	Crystalline stem length, l^{*c} (nm)	Crystalline stem length, l_R^{*d} (nm)
		DSC[e] (wt%)	Density (wt%)				
H-1	132.2	72.7	73.2	23.5	16.3	20	25.8
H-2	131.8	73.3	73.3	23.3	16.3	19.5	24.7
H-3	129.3	62.6	64.0	22.2	13.1	16.4	20.6
H-4	132.6	67.7	72.8	24.4	15.7	20.7	26.9
H-5	132.9	60.9	70.8	26.0	14.8	21.2	25.8
U-1	130.9	48.9	54.3	33.3	16.1	18.2	24.8
U-2	130.3	49.6	54.9	33.3	16.5	17.4	23.8
L-1	113.2	46.3	50.1	13.2	5.6	8.1	10.8
L-2	111.1	44.4	50.4	12.8	5.2	7.6	10.3
L-3	107.9	40.4	47.7	12.3	4.5	6.9	9.7
L-4	108.8	40.0	47.7	11.6	4.2	7.1	9.7
L-5	105.9	40.0	46.6	11.0	4.0	6.6	8.6
LL-1	114.1	43.0	47.5	13.9	5.5	8.3	11.0
LL-2	121.0	41.6	47.3	16.1	6.1	10.7	12.1
E-1	96.6	30.1	35.9	11.5	3.1	5.4	8.4
E-2	60.6	10.9	11.9	11.0	1.0	3.1	6.4

[a] Estimated from SAXS.
[b] Calculated from long period (SAXS) and crystallinity (DSC): $L_c = LP/X_c^{vol}$, where $X_c^{vol} = X_c/[(\rho_c/\rho_a)(1-X_c)+X_c]$; $\rho_c = 1.0$ g/cm^3 and $\rho_a = 0.85$ g/cm^3 are the densities of crystalline and amorphous phase, respectively.
[c] Calculated on the basis of temperature of the melting peak (DSC).
[d] Calculated from Raman spectra (position of LAM-1 peak).
[e] Estimated on the basis of the heat of melting (DSC).

displacement of the plunger and $CR = h_0/h$ is the compression ratio.

Fig. 4(a)–(c) show representative true stress-true strain curves determined for polyethylene samples studied in this work. These curves were obtained for specimens deformed continuously in a die with the initial deformation rate of $8.3\times10^{-4}\,s^{-1}$ (5%/min) at room temperature. Compression was carried out up to either the fracture of the specimen or approach of the load limit of the loading frame (5 T), whichever happened earlier.

As expected, the shape of the curves is similar to a typical compression curve-there is no local stress (load) maximum

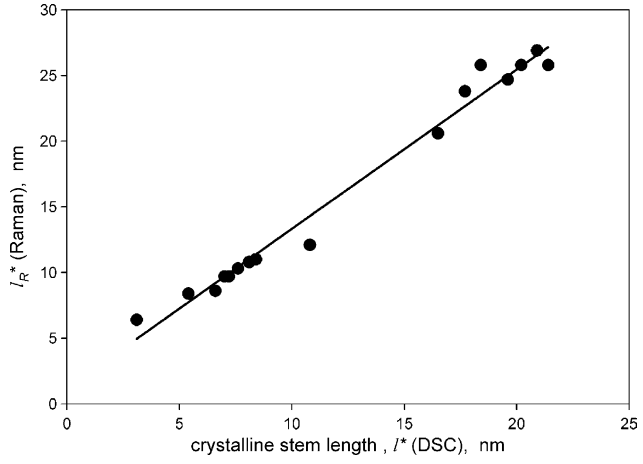

Fig. 3. Correlation between crystalline stem length, l^*, as evaluated from DSC and Raman spectroscopy measurements.

near the yield point and the plastic flow is followed by an intense strain hardening stage. Moreover, the shape of the presented curves agrees quite well with the true stress-true strain curves obtained in tensile deformation mode for the samples of polyethylene of similar molecular characteristics [12,34]. The yield and flow stresses observed in compression are slightly higher as compared to tension. The main difference between tensile and compression curves are, however, in the strain hardening stage: The samples tested in tension did not show such a strong strain hardening as observed here. Besides, they used to fracture in tension at lower strains than in the compression mode. For example, linear polyethylene similar to samples H-1 and H-2 studied here, fractured in tension at the true strain below 2.0, while the stress approached 200 MPa [12]. In contrast, samples H-1 and H-2 tested in the plane-strain compression demonstrated the stress near 300 MPa at the respective strain, and moreover could be deformed further to higher strain and stress levels (at $e = 2.1$ the true stress was around 500 MPa and no fracture happened up to this point). Such a difference in strain hardening behavior results most probably from the fact that the plane-strain compression produces much less fragmentation of lamellae than does the tension [18], in which the entire lamellar structure is destroyed and replaced by micro-fibrils. Simultaneously, micro-cavitation, while severe in tension, is strongly suppressed in the compression mode of deformation. Both features result from the presence of external constraints in the plane-strain compression, generating compressive stress component. Consequently, the already highly strained lamellar crystals as well as

highly extended amorphous material within amorphous layers are much more constrained than in tension and the sample responds to compression with higher stress than on extension to the same strain. Due to the inhibition of cavitation, the compressed, still continuous material can deform to higher strains than in the tensile mode in which numerous cavities act as flaws leading to the premature fracture.

The true stress-true strain curves determined for the samples of linear polyethylene of various molecular mass and crystallinity, shown in Fig. 4(a), demonstrate that the elastic modulus, the stress at yield point and the stress accompanying plastic flow increase gradually with increasing crystallinity of the material, while the strain hardening stage depends primarily on the molecular weight of a polymer rather than on the properties of crystalline component. It can be seen that the onset of strong strain hardening shifts noticeably to lower strain with an increasing molecular weight. At the same time, the rate of that strain hardening increases, although this increase is not as pronounced as the depression of the onset point. Since the stress hardening is controlled primarily by the orientation of the amorphous network of entangled chains [35] such a behavior demonstrates that its properties, including density of the entanglements, in semicrystalline polymer depend on the molecular weight, which is opposite to amorphous polymers or polymer melts.

Branched polyethylene samples (Fig. 4(b)) exhibit lower modulus as well as yield and flow stresses than linear species due to lower fraction of crystalline component and smaller dimensions of crystallites. Moreover, they demonstrate less strain hardening and usually fracture at true strain below 2.0. Nevertheless, the strain hardening behavior seems to depend again on molecular weight of the polymer, similarly to linear polymers: The onset shifts to lower strain, while the rate of strain hardening increases with an increasing molecular mass. The second factor influencing stress-hardening behavior is the degree of branching: For a comparable molecular weight (samples L-1, L-2, L-4) higher branching results in a higher rate of strain hardening. The strain at which branched polymers fracture also depends on both molecular weight and the level of branching. This ultimate strain apparently increases with an increasing molecular weight, as in linear species, and decreasing degree of branching. The chains containing long branches are most probably more constrained than the linear chains within the molecular network since long branches entangled with other chains constitute a serious hindrance for reptation of a branched chain. This results in the formation of an entanglement network less tractable than that formed by linear chains of a comparable molecular weight. This, in turn, limits the ability of the polymer to large strain deformation and causes its earlier fracture. From this point of view, the constitution of entanglement network, modified by the presence of long branches, seems to be an

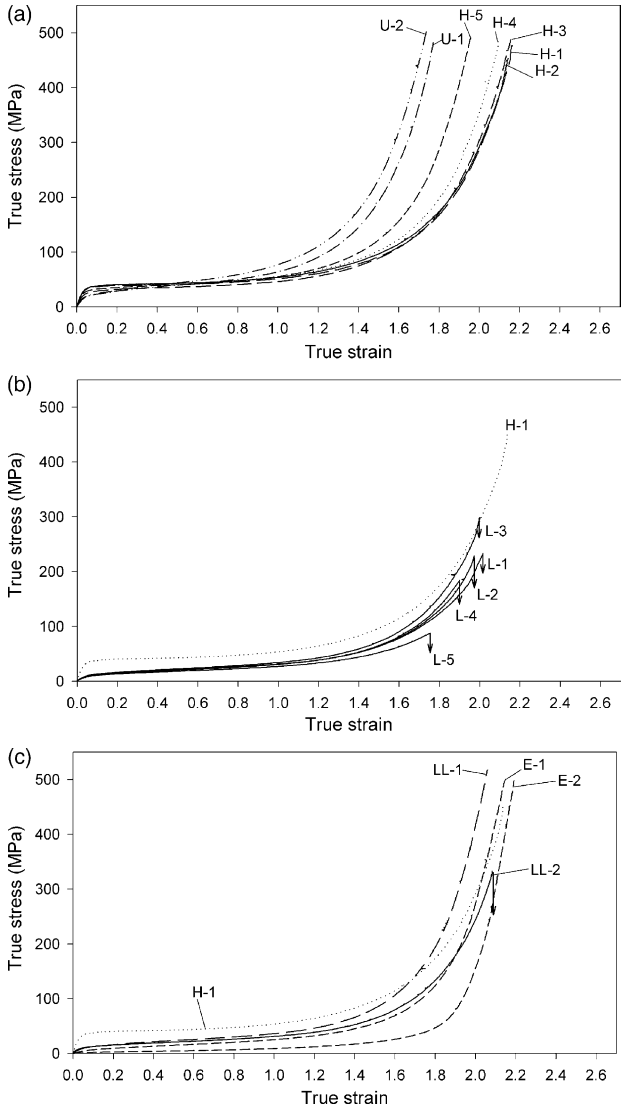

Fig. 4. Representative true stress-true strain curves obtained in the plane-strain compression: (a) Linear polyethylenes, (b) branched polyethylenes, (c) copolymers. All deformation experiments were performed at room temperature and initial deformation rate of 0.00083 s^{-1}. In (b) and (c) the curve of linear polyethylene H-1 is plotted as a reference (dotted line).

essential factor controlling not only strain hardening but also the fracture behavior.

The features of the stress–strain curves observed for ethylene-based copolymers, presented in Fig. 4(c), are similar to those of linear polyethylenes. These copolymers are essentially linear, with only short side branches distributed quite uniformly along the chain, thus the strain hardening behavior of such copolymers resembles that of linear polyethylene, including its dependence on molecular mass. The modulus and yield stress, controlled primarily by crystalline component are lower than in the linear polyethylene, due to lower crystallinity as well as smaller size of crystallites. The copolymers studied can deform to high strains, with generation of high stress and no tendency to premature fracture. An exception is the sample LL-2,

which is a linear low-density polyethylene, produced with Ziegler–Natta catalyst. Such technology usually effects in macromolecules with more heterogeneous distribution of comonomer than in the case of metallocene technology (LL-1, E-1, E-2). This heterogeneous chain structure is probably responsible for a lower fracture strain of LL-2 comparing to homogeneous metallocene-based copolymers.

It is worth noting that the stress generated on strain hardening is exceptionally high even in the sample of E-1 elastomer, which exhibits very low crystallinity (below 12 wt%). This demonstrates that the contribution of stretching of the entanglement network of the amorphous phase to the strain hardening process is very substantial, practically dominant.

As it was already mentioned, the initial stages of plastic deformation in the plane-strain compression are controlled by the amount of amorphous and crystalline components in the sample and by the properties of crystallites. This is shown by Figs. 5 and 6, showing the evolution of elastic modulus and yield stress, respectively. Fig. 5 demonstrates that the fraction of amorphous phase appears to be a principal parameter controlling the elastic modulus. In fact, we have not found any clear correlation of Young's modulus with other parameters describing amorphous or crystalline phase like, e.g. the length of crystalline sequence-in all cases data scattered much stronger than on the plot of modulus vs. concentration of the amorphous phase. In general, a dependence presented in Fig. 5 is similar to that reported in literature ([36,37]). The elastic modulus decreases monotonically with decreasing overall crystallinity of the sample. The actual dependence seems to be complex, thus the line was plotted merely to show a trend rather than to propose any particular form of the curve. Note, that we did not take into account any dependence of the modulus of the crystalline phase on the size of the unit cell, which actually can vary slightly, especially in the samples of copolymers, or a possible influence of variation of supermolecular structure. Discussion of these is, however, beyond the scope of this study.

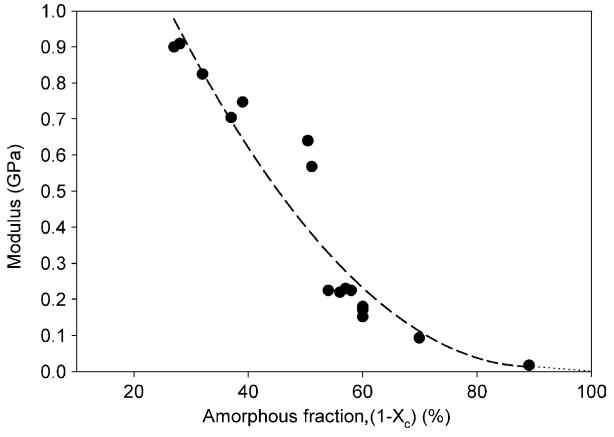

Fig. 5. The plot of Young's modulus as a function of content of amorphous component in the sample.

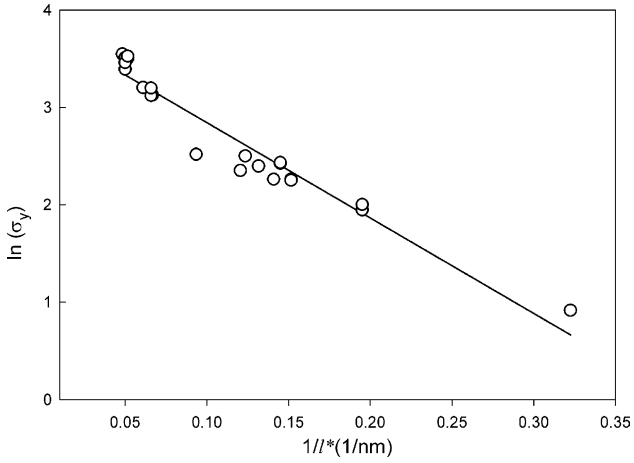

Fig. 6. The dependence of the yield stress on the length of crystalline sequence in lamellar crystals, l^*.

Crist et al. [37] hypothesized that such a substantial dependence of the modulus on phase structure can be explained as being a result of strong dependence of the modulus of amorphous phase, E_a, on crystal thickness L_c through modification of mechanical α_1 relaxation process in the vicinity of the interface, in addition to mixing rules.

The modulus-phase composition dependence can be extrapolated to extremely low value of Young's modulus for a fully amorphous sample ($X_a = 100\%$, $X_c = 0$). This is reasonable, since deformed polyethylene was more than 120 K above its glass transition temperature, so that in the absence of crystals the completely amorphous sample should behave as a melt, with a rubber-like elasticity manifested through entanglements. Extrapolation of the experimental data obtained for melts and series of low-crystallinity model copolymers, done by Krigas et al. [38] yielded, in fact, a very low modulus for completely amorphous sample, $G_a \sim 1$–2 MPa (corresponding to $E_a \sim 2$–5 MPa). On the other hand, it was postulated [37] that for highly crystalline samples, E_a can increase up to approximately 300 MPa due to the influence of adjacent crystalline layers on α_1 mechanical relaxation process.

Fig. 6 presents the evolution of the yield stress. Since we did not observe any maximum on the load-displacement curve, the yield stress was estimated using a 2% offset construction. The yield point evaluated in such a way coincides well with the onset of plastic deformation deduced from strain recovery data, discussed in the companion paper [19]. Fig. 6 demonstrates that the yield data can be correlated in a broad range with the length of crystalline sequence, l^*, in the lamellar crystal. On the other hand, no satisfactory correlation between the yield stress and crystallinity was found. The semi-logarithmic plot of the yield stress vs. $1/l^*$ gives a straight line, suggesting a dependence of the type $\sigma_y \sim A \exp(-B/l^*)$, where A and B are constants. Such type of equation can be expected on the basis of the dislocation model proposed by Young [39] and Crist [40], developed further by Brooks et al. [41]. According to this

hypothesis, the mechanisms controlling the yield behavior of semicrystalline polymer is thermal nucleation of screw dislocations within the crystalline phase. Generation of such screw dislocations is necessary to activate plastic deformation by crystallographic slip mechanisms. At this stage, the contribution of an amorphous component to plastic deformation is very limited. The principal role of amorphous material is to transmit load to the crystalline lamellae [35]. Similarly to Young's modulus, we do not discuss here any possible influence of the supermolecular structure or the size of the unit cell on the yield stress. In particular, any change of the interplanar distance could modify the critical resolved shear stress of the crystallographic slip and, therefore, also the yield stress. Such dependencies can be a source of some scatter of the data in the plot of Fig. 6 and certainly should be taken into account in a more detailed analysis.

3.3. Molecular network properties

In order to learn more from the stress–strain curves, especially about properties of the molecular network, some model calculations were performed. Haward and Thackray [42] suggested many years ago that the deformation of a polymer can be modeled by a simple constitutive model consisting of a Hookean spring, used to characterize the initial elastic response, connected in series with a dashpot being in parallel with another non-linear spring. A viscoplastic dashpot represents the rate and temperature dependent yield and plastic flow, while the second, non-linear rubber elasticity spring accounts for an anisotropic resistance to molecular orientation which develops with plastic strain. According to Haward's hypothesis, strain hardening originates from stretching of the molecular entanglement network which is represented in the model by the non-linear spring element. Such an approach is supported by a complete reversibility of deformation when deformed amorphous polymers are brought above their glass transition temperature. This simple constitutive model as well as more sophisticated 3D models based on original Haward's hypothesis were successfully applied to model stress–strain behavior of several amorphous as well as semicrystalline polymers under various conditions of load [43–48]. Therefore, we decided to apply this concept for modeling our experimental curves. Since the primary interest was in the response of the molecular network, several simplifying assumptions were done: the material was assumed incompressible and the initial elastic deformation was neglected, as the respective strain is small comparing to the total strain. Next, the viscoplastic response was reduced to purely plastic, represented by the plastic flow stress alone. Any dependence on the strain rate and temperature was also neglected. Moreover, we did not take into account any molecular relaxation phenomena within the network, which in the real system can accommodate some part of the imposed deformation. Under such assumptions the true stress generated in the system can be simply represented by the sum (dashpot and spring in parallel) [45]:

$$\sigma = Y + \sigma_R \tag{5}$$

where Y is the plastic flow stress and σ_R is the rubber-like stress generated by the entangled molecular network.

The network stress σ_R was modeled using a non-Gaussian chain statistics and the 8-chain model developed by Arruda and Boyce [49], which has been found to accurately capture the state of strain dependence of the stress–strain behavior of elastomers and glassy polymers. For the plane-strain geometry, the equation for the stress in the direction of loading takes the form:

$$\sigma_R = \frac{N_e kT}{3}\sqrt{n}\frac{1}{\lambda_{chain}}L^{-1}\left(\frac{\lambda_{chain}}{\sqrt{n}}\right)\left(\lambda^2 - \frac{1}{\lambda^2}\right) \tag{6}$$

where N_e is the effective crosslinks density, n is the number of 'rigid links' between cross links (entanglements) providing limiting extensibility of a chain ($\lambda_{max} = n^{1/2}$) and λ_{chain} is the stretch on each chain in the network, given by the root mean square of the applied strain; for plane strain compression $\lambda_{chain} = [(\lambda^2 + 1 + 1/\lambda^2)/3]^{1/2}$, where $\lambda = CR = h_0/h$ is the compression ratio. The quantity $N_e kT$ is equivalent to the initial strain hardening modulus of the network, G_n. $L^{-1}(x)$ denotes the inverse Langevin function ($L(x) = \coth(x) - 1/x$; here $x = \lambda_{chain}/n^{1/2}$), which can be accurately approximated by Pade approximation [45,50]:

$$L^{-1}(x) = x\frac{3 - x^2}{1 - x^2} \tag{7}$$

It should be noted that for large values of n, Eq. (6) reduces to the Gaussian equation and becomes (neo-Hookean solid deformed in the plane-strain conditions):

$$\sigma_R = N_e kT\left(\lambda^2 - \frac{1}{\lambda^2}\right) \tag{8}$$

Using Eq. (5) substituted with (6) and (7) the experimental true stress-true strain curves, presented in Fig. 4, were fitted in the strain range of $e = 0.1$–2.0. The parameters of the fit were a disposable flow stress Y, the effective cross-link density N_e, and the number of rigid links between entanglements n.

Fig. 7 presents a few exemplary results of fitting procedure obtained for linear polyethylenes. The fits obtained for other samples demonstrated similar features and quality. It can be seen that the obtained fits were reasonably good up to the true strain of $e = 1.2$–1.5. For higher strains, the calculated true stress rises much faster than that observed experimentally. This discrepancy must be accounted primarily for simplifying assumptions done for calculations, especially the one neglecting relaxation of the network. Another observation is that for the true strain below 0.7 the fitted curves demonstrated very low sensitivity on an increase of parameter n, which implied

that the experimental curves could be successfully approximated also with the Gaussian Eq. (8). In fact, if the true stress was plotted against λ^2-1/λ^2 the experimental curve could be easily approximated with a straight line up to $(\lambda^2-1/\lambda^2)=4$–5, i.e. for $e<0.7$–0.8, which means that the neo-Hookean description is valid in this strain range. This is illustrated by the inset in Fig. 7. The slope of respective straight line gives directly the network modulus $G_n=N_ekT$.

Table 3 summarizes the values of effective network density N_e, initial strain hardening modulus of the network, G_n, and the average number of rigid segments between entanglements, n, derived from fitting. The values obtained for N_e and G_n are most probably quite rational (the same values were obtained by both non-Gaussian and Gaussian fits; G_n shows up in the low and moderate strain portion of the curve, where all effects neglected in calculations are not critical yet). The obtained values of G_n agree with those found for PE by other authors [8,12,44]. However, the obtained values of n can be a bit more uncertain, since the fitted curves are most sensitive to this parameter in the range of moderate and high strain, where the model is much less precise due to all simplifications done. To improve that, a more sophisticated and precise model should be applied (e.g. similar to that proposed in Ref. [51]). On the other hand, for most of determined N_e and n pairs their product is roughly constant, as can be expected for networks of chains of similar flexibility, which may suggest validity of the calculations.

From the network density N_e the average molecular mass between cross-links, M_e, can be calculated using the following equation [11]:

$$N_e = \frac{\rho N_A}{M_e}\left(1-\frac{2M_e}{M_n}\right) \tag{9}$$

Table 3
Parameters of the network determined from fitting of experimental stress–strain curves

Sample	$N_e\times10^{-26}$ (1/m^3)	G_n (MPa)	M_e (g/mol)	n
H-1	4.49	1.8	1020	22.0
H-2	4.71	1.9	986	21.0
H-3	4.49	1.8	1093	20.0
H-4	4.92	2.0	981	18.5
H-5	5.56	2.3	898	13.8
U-1	9.63	3.9	543	12.5
U-2	12.62	5.1	414	12.8
L-1	3.64	1.5	1376	22.5
L-2	3.96	1.6	1281	23.0
L-3	4.49	1.8	1091	22.0
L-4	3.96	1.6	1256	21.5
L-5	3.38	1.4	1250	31.0
LL-1	4.92	2.0	1033	22.5
LL-2	4.06	1.6	1158	25.5
E-1	3.85	1.6	1211	25.5
E-2	1.60	0.6	2951	25.0
PE melt				1240[a]

[a] From Ref. [52].

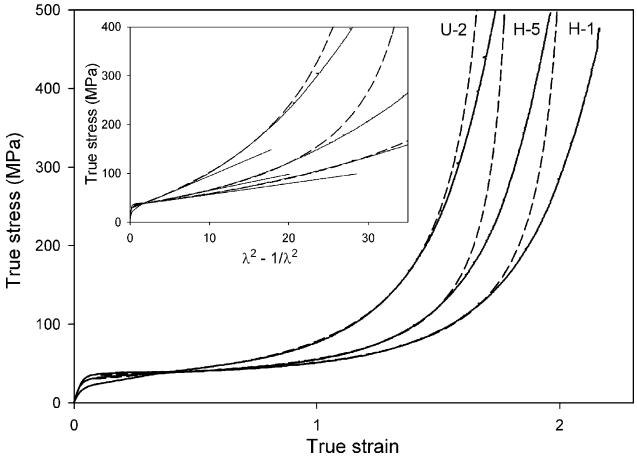

Fig. 7. Experimental and fitted true stress-true strain curves (solid and dashed lines, respectively) of representative samples of linear polyethylene. Inset shows the same stress data plotted in the neo-Hookean coordinates.

where ρ is the density of amorphous phase, N_A is the Avogadro number and M_n is the number average molecular weight. The second term in the brackets is the Flory correction term for dangling chain ends. The calculated values of M_e are also presented in Table 3 and compared with the respective value reported for PE melt [52].

All determined parameters show some dependence on both molecular weight and crystallinity. The dependence on crystallinity (an increase of N_e and G_n and a decrease of n with increasing crystallinity), is roughly linear and not very strong, especially that for G_n or N_e. Most probably, it accounts for an increasing number of chains immobilized by crystallites (tie-molecules, cilia) with increasing crystallinity. These crystal-amorphous junctions act as physical solid cross-links supplementary to cross-links produced by entanglements. In addition to the above dependence on crystallinity, a significant dependence of evaluated parameters on molecular weight can also be observed. This dependence is shown in Fig. 8. One can observe in this Figure that both G_n and n data, when plotted against molecular weight, tend to group along two separate curves-one for linear PE's of relative high crystallinity, and the other for branched PE and copolymers of lower crystallinity, which reflects the already mentioned dependence on crystallinity. However, it is possible to 'reduce' G_n and n values to the same crystallinity level (say 50%) using the linear dependence of both parameters on crystallinity, as estimated from the respective data. After such a recalculation the G_n or n parameters estimated for all samples define a single curve when plotted against molecular weight. This is shown by Fig. 9 showing the plot of such 'reduced' network modulus. A similar single curve can be obtained for parameter n (plot not presented here).

Such a dependence of network properties on molecular weight has been never observed for amorphous polymers or polymer melts in which the density of entanglements is controlled primarily by chain

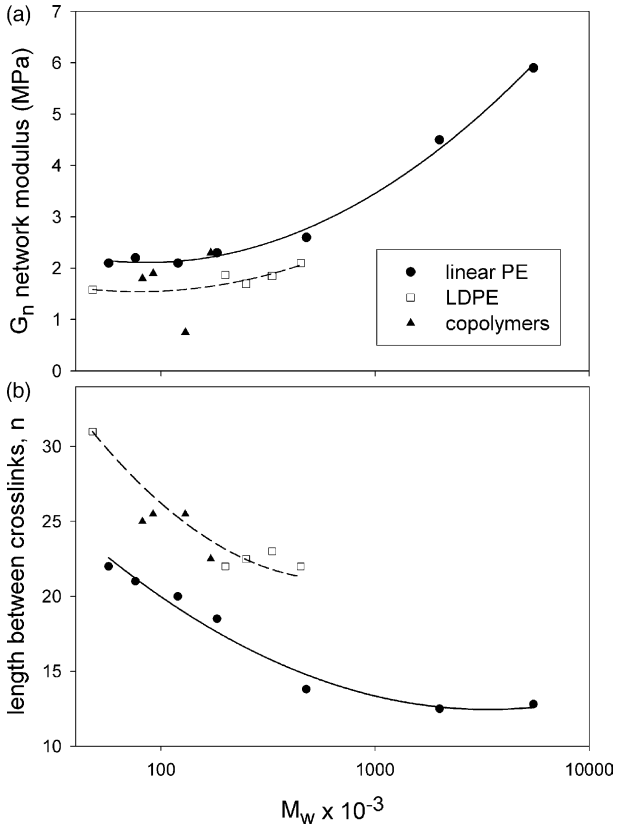

Fig. 8. Network modulus (a) and the average number of segments between cross-links (b) obtained from fitting, plotted against molecular weight of the sample.

architecture and flexibility [11]. However, that behavior can be expected for solid semicrystalline polymers since during crystallization at usual conditions only part of the entanglements present in the melt can be resolved, while all remaining are rejected by growing crystallites into amorphous layers. As a consequence, the density of entanglements in the amorphous component must differ from that in the melt prior to crystallization and frequently can be even considerably higher than that in the melt. With increasing molecular weight the fraction of resolved entanglements decreases since the time necessary for diffusion through reptation tube of increasing length also increases ($\tau_r \propto M^3$; according to Ref. [53] reptation time increases from 0.15 to 132 s when molecular weight increases from 10^5 to 10^6) and frequently becomes longer than the accessible time set by crystallization kinetics, generally independent of M (in cooling conditions applied in this work, crystallization is completed within seconds). This, in turn, leads to an increase of the number of entanglements, which have to be redistributed into amorphous layers. Consequently, the local density of entanglements in the amorphous component should increase with an increasing molecular weight as in the case reported here. Similar behavior was recently reported for linear PE and PP [8]. Additionally, we should note that the estimated density of cross-links N_e contains also a contribution of solid physical cross-links introduced by crystallites through chains crossing a crystal-amorphous interface (tie-molecules, cilia), which as already discussed depends on the crystallinity and morphology of crystals.

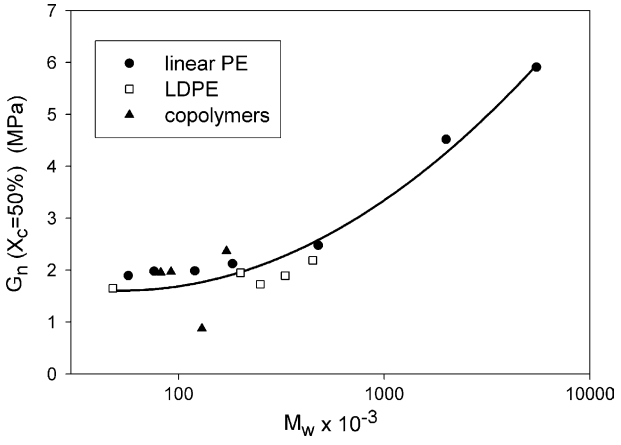

Fig. 9. The dependence of network modulus G_n expected for samples of 50% crystallinity on their molecular weight.

The model calculations reported above indicate that the evolution of the strain hardening behavior with molecular weight can be interpreted in terms of modification of the molecular network properties related to the crystallization process and its kinetics.

4. Conclusions

Results of the reported study demonstrate that the deformation behavior at low strains, including the yield range, is governed by properties of the crystalline phase. The key parameter controlling the yield is most likely the length of crystalline stem determining the rate of nucleation of dislocations, which are elementary carriers of plastic deformation by crystallographic slip mechanisms. The amorphous layers, although more compliant than crystallites, are intimately connected to and strongly constrained by adjacent lamellae and can deform only cooperatively with them to accommodate the strain. Thus, the role of the amorphous component at this stage of deformation is limited to transfer the load to and between crystallites. The situation changes at higher strains, when stresses generated by stretching of the network of entangled chains within the sheared amorphous layers become higher than those accompanying deformations of the crystalline component. Consequently, the stage of strain hardening is a property of the amorphous component. The obtained results confirm that the strain hardening stage is controlled primarily by the properties of the network of entangled chains of the amorphous component. The rubber-elasticity of the molecular network, manifesting itself in the strain hardening behavior, is determined by the density of cross-links, produced by chain entanglements and chains immobilized

on the crystal-amorphous interface. These in turn, as demonstrated by model calculations, appear to depend on molecular weight, crystallization kinetics and resultant crystallinity of the sample. The higher molecular weight and/or crystallization rate, the larger density of the entanglements. Also the chain architecture, i.e. the presence of long or short branches or comonomer units, modifies the density of the network, which is finally shaped upon crystallization. All that makes the amorphous component of semicrystalline polymers significantly different than amorphous polymers, where the density of chain entanglements depends neither on molecular weight nor thermal history of the sample.

Acknowledgements

Grant 7 T08E 036 19 from the State Agency for Scientific Research of Poland is acknowledged for partial financial support of this work. BASF Polska and Ticona GmbH are acknowledged for kind supply of polymers used in this study.

References

[1] Ward IM. In: Ward IM, editor. Structure and properties of oriented polymers. London: Chapman & Hall; 1977.
[2] Bowden PB, Young R. J Mater Sci 1974;9:2034–51.
[3] Lin L, Argon AS. J Mater Sci 1994;29:294–323.
[4] Oleinik EF. Polym Sci Ser C 2003;45:17–117.
[5] Strobl G. The physics of polymers. Concepts for understanding their structures and behavior. New York: Springer; 1997.
[6] Bastiaansen CWM, Meyer HEH, Lemstra PJ. Polymer 1990;31:1435–9.
[7] Lemstra PJ, Bastiaansen CWM, Rastogi S. In: Salem DR, editor. Structure formation in polymeric fibres. Munich: Hanser; 2000.
[8] Schrauwen BAG, Janssen RPM, Govaert LE, Meijer HEH. Macromolecules 2004;37:6069–78.
[9] Smith P, Chanzy HD, Rotzinger BP. Polym Commun 1985;26:258–60.
[10] Maxwell AS, Unwin AP, Ward IM. Polymer 1996;37:3293–301.
[11] Flory PJ. Principles of polymer chemistry. New York: Cornell University Press; 1953.
[12] Hiss R, Hobeika S, Lynn C, Strobl G. Macromolecules 1999;32:4390–403.
[13] Hobeika S, Men Y, Strobl G. Macromolecules 2000;33:1827–33.
[14] Fu Q, Men Y, Strobl G. Polymer 2003;44:1927–33.
[15] Fu Q, Men Y, Strobl G. Polymer 2003;44:1941–7.
[16] Men Y, Strobl G. J Macromol Sci Phys 2001;B40:775–96.
[17] Al-Hussein M, Strobl G. Macromolecules 2002;35:8515–20.
[18] Galeski A, Bartczak Z, Argon AS, Cohen RE. Macromolecules 1992;25:5705–18.
[19] Bartczak Z. Polymer, in press.
[20] Hoffman JD. Polymer 1983;24:3–26.
[21] Hoffman JD. Polymer 1982;23:656–70.
[22] Wunderlich B, Czornyj G. Macromolecules 1977;10:906–13.
[23] Hoffman JD, Miller RL. Polymer 1997;38:3151–212.
[24] Psarski M, Piorkowska E, Galeski A. Macromolecules 2000;33:916–32.
[25] Brandrup J, Immergut EH, Grulke EA, editors. Polymer handbook. 4th ed. New York: Wiley; 1999.
[26] Schaufele RF, Schimanouchi T. J Chem Phys 1967;47:3605–10.
[27] Rastogi S, Spoelstra AB, Goossens JGP, Lemstra PJ. Macromolecules 1997;30:7880–9.
[28] Crist B, Rafner MA, Brower AJ, Sabin RJ. J Appl Phys 1979;50:6047–51.
[29] Snyder RG, Krause SJ, Schere JR. J Polym Sci, Part B: Polym Phys Ed 1978;16:1593–609.
[30] Young RJ, Bowden PB, Ritchie JM, Rider JG. J Mater Sci 1973;8:23–36.
[31] Lacks DJ, Rutlege GC. J Phys Chem 1994;98:1222–31.
[32] Nakamae K, Nishino T, Ohkubo H. J Macromol Sci Phys 1991;B30:1–23.
[33] Basset DC, Hodge AM. Proc R Soc London A 1981;377:25–9.
[34] G'Sell C, Hiver J, Dahoun A, Souahi A. J Mater Sci 1992;27:5031–9.
[35] Lee BJ, Argon AS, Parks DM, Ahzi A, Bartczak Z. Polymer 1993;34:3555–75.
[36] Popli R, Mandelkern L. J Polym Sci, Part B: Polym Phys 1987;25:441–83.
[37] Crist B, Fisher CJ, Howard PR. Macromolecules 1989;22:1709–18.
[38] Krigas T, Carella JM, Struglinski MJ, Crist B, Graessley WW, Schilling FC. J Polym Sci, Part B: Polym Phys 1985;23:509–20.
[39] Young RJ. Mater Forum 1988;11:210–8.
[40] Crist B. Polym Commun 1989;30:69–71.
[41] Brooks NWJ, Mukhtar M. Polymer 2000;41:1475–80.
[42] Haward RN, Thackray G. Proc R Soc London A 1967;302:453–72.
[43] Boyce MC, Parks DM, Argon A. Mech Mater 1988;7:15–33.
[44] Haward RN. Macromolecules 1993;26:5860–9.
[45] Haward RN. Polymer 1999;40:5821–32.
[46] Buckley CP, Jones DC, Jones DP. Polymer 1996;37:2403–3414.
[47] Boyce MC, Socrate S, Llana PG. Polymer 2000;41:2183–201.
[48] van Dommelen JAW, Parks DM, Boyce MC, Brekelmans WAM, Baaijens FPT. J Mech Phys Solids 2003;51:519–41.
[49] Arruda EM, Boyce MC. J Mech Phys Solids 1993;41:389–412.
[50] Cohen A. Rheol Acta 1991;30:270–3.
[51] Hong K, Rastogi A, Strobl G. Macromolecules 2004;37:10165–73.
[52] Pearson DS, Fetters LJ, Graessley WW, Strate GV, von Meerwall E. Macromolecules 1994;27:711–9.
[53] Barham PJ, Sadler DM. Polymer 1991;32:393–5.